

Chip-Based Chiral 3D Metamaterial with Functional Core-Shell Architecture for Femtomolar Biodetection

Mariachiara Manoccio

Università del Salento

Marco Esposito

CNR Nanotec

Elisabetta Primiceri

CNR Nanotec

Angelo Leo

CNR Nanotec

Vittorianna Tasco (✉ vittorianna.tasco@nanotec.cnr.it)

CNR <https://orcid.org/0000-0002-3392-0976>

Massimo Cuscunà

CNR-Nanotec

Dmitry Zuev

ITMO University

Yali Sun

ITMO University

Giuseppe Maruccio

Scuola Superiore Isufi, Università del Salento

Alessandro Romano

Division of Neuroscience, Institute of Experimental Neurology, San Raffaele Scientific Institute

Angelo Quattrini

San Raffaele Scientific Institute, Milan, Italy

Giuseppe Gigli

CNR - Nanotec

Adriana Passaseo

Institute of Nanotechnology-National Research Council <https://orcid.org/0000-0002-1845-4073>

Article

Keywords: Biomarkers, Plasmonic Sensors, Molecular Tracking Solutions, Circular Dichroism Spectrum, Neurodegenerative Disease Screening

Posted Date: July 15th, 2021

DOI: <https://doi.org/10.21203/rs.3.rs-275766/v1>

License:  This work is licensed under a Creative Commons Attribution 4.0 International License.

[Read Full License](#)

Abstract

Advanced sensing tools capable to detect extremely low concentrations of circulating biomarkers can open unexplored routes towards early diagnostics of diseases and their progression monitoring. Plasmonic sensors are an emerging technology enabling different optical effects that can be used as molecular tracking solutions. Here we demonstrate the sensing capabilities of a chip-based metamaterial, combining the 3D chiral geometry with an optically functional core-shell architecture. The sensor can be easily handled and exhibits reliability and stability during the whole functionalization and analytical procedure thanks to the on-chip format. The system shows a linear shift of circular dichroism spectrum upon interaction with different concentrations of TAR DNA-binding protein TDP-43, a clinically relevant biomarker for neurodegenerative disease screening. The measurements were performed in spiked solution as well as in human serum, with concentrations from 1pM down to 10fM, a range not accessible with commonly used immunological assays and that can thus open new perspectives for disease knowledge and early diagnostics.

Introduction

In biomedical research and clinical practice there is a huge demand of high performance sensors for advanced diagnostics and real-time monitoring of disease evolution^{1,2}, outperforming and simplifying standard approaches, such as real-time polymerase chain reaction (RT-PCR) and the enzyme-linked immunosorbent assay (ELISA). Continuous technological improvements are required to increase sensitivity, specificity, and accuracy towards the challenging detection of small-size molecules or ultra-low concentration target analytes. In the last years, artificially engineered optical devices exploiting plasmonic properties, emerged as good candidates to be implemented as low-cost, miniaturized and multiplexing biosensors^{3–8}. Plasmonic biosensors are mostly based on the surface plasmon resonance (SPR) along metal/dielectric interfaces, and on the localized surface plasmon resonance (LSPR) occurring in nanostructures. Both detection mechanisms are strongly sensitive to the refractive index changes of the surrounding medium, within their respective plasmon decay lengths. Generally, SPR sensors exhibit higher sensitivity than LSPR, but require more complex excitation optics (such as prism or grating coupling) and extended smooth surfaces.

In order to improve the sensor performances, one strategy consists in the material and shape engineering of plasmonic nanostructures^{9–11}. In particular, the addition of anisotropy to plasmonic nanoobjects could enable novel degrees of freedom and polarization dependence in the optical response and, consequently, new biosensing concepts. One example are chiral plasmonic nanostructures^{12,13}, characterized by the absence of the mirror symmetry, which exhibit handedness and behave differently when interacting with circularly polarized light (CPL). In this respect, the circular dichroism (CD) spectroscopy, defined as the differential measurement of optical absorption in chiral enantiomers upon interaction with left and right-handed CPL^{14,15}, has a huge potential in the biosensing field because of its differential nature, free from background noise, and for the presence of several spectral features, other than the typically broad

plasmonic resonances. Indeed, recent studies reported the modelling and fabrication of chiral plasmonic metamaterial with various morphologies mostly for enantiomeric detection, based on the plasmonic driven amplification of natural occurring CD signals^{16–21}. The employment of chiral plasmonic elements to detect changes in the surrounding medium induced by target analyte presence is mainly limited to few works, employing chiral nanoparticles dispersed in solution^{22–25}. However, in view of developing novel biosensing schemes of practical employment towards portable point of care devices, a chip-based approach with sensing nanostructures, organized with a long-range order and integrable in photonic circuits, rather than dispersed in solution, would significantly impact the spread of such a technology²⁶. It will offer great advantages in terms of repeatability, integration with microfluidics components and stability against different solvent and salt concentration, that can instead induce precipitation if colloidal nanoparticles are used. Furthermore, the chip-based format is particularly suitable for analytical procedures, allowing easy washing steps that are essential for real application with complex biological samples, rather than simpler protein solutions^{27,28}.

In the present work, we demonstrate the possibility to exploit a chip-based approach for chiral sensing technology through compact helix metamaterial arrays, engineered with a functional metallic core/dielectric shell composition. As dielectric shell we have used the same polymer-mediated surface functionalization layer, needed for high-yield and specific biorecognition of any type of biomolecule. Such a composite structure, modifying the metamaterial far-field and near-field response, leads to a more efficient interaction and detection of biomolecules, as compared to other bioconjugation schemes. The device is used to detect a neurodegenerative related biomarker, for which specificity and detection up to the femtomolar range are demonstrated in controlled solutions as well as in complex human fluids.

The scheme of our biosensor is shown in figure 1. The engineered building block, grown by Focused Ion Beam Induced Deposition (FIBID)²⁹, consists of a periodic array of chiral core-shell nanostructures, where the single element is a free-standing metallic helix, that, given the 3D nature, can have the additional advantage of increasing the available binding surface exposed to the analyte³⁰. The chiral metamaterial is then prepared for biochemical functionalization through the conformal coverage with an ultrathin dielectric polymeric shell, the Poly-o-phenylenediamine (P-oPD). Such an approach is chemically simple, cost-effective and time-saving, while ensuring stability, effective coverage and selectivity of the sensing nanostructures especially for analysis of complex biological matrix³¹. The resulting core-shell architecture, with respect to dielectric function profile, represents the key element to achieve high sensitivity, because, on one side, it offers an ideal surface coverage for high stability molecular immobilization onto the 3D nanohelices, while, on the other side, it allows to enhance the near- and far-field optical response of the nanohelices.

After antibody covalent binding, we applied our engineered sensing device against variable concentration of the transactive response (TAR) DNA-binding protein 43 (TDP-43), a distinctive protein of amyotrophic lateral sclerosis (ALS) and frontotemporal lobar degeneration (FTLD)^{32,33}. Currently, the diagnosis of these neurodegenerative diseases is still clinically-based and no biomarkers have yet been routinely

incorporated into the clinical practice or clinical trials. TDP-43 is the main component of the pathological inclusions found in the cytoplasm of neurons and glial cells of the majority of ALS and Tau-negative FTLD cases. As a consequence TDP-43 has been largely proposed and studied as a potential biomarker for ALS and FTLD. Increased level of TDP-43 protein was found in cerebrospinal fluid (CSF) and plasma of patients with ALS and FTLD³⁴ using mass spectrometry³⁵, Western Blot and ELISA analysis^{36,37}. However, the extremely low concentration of TDP-43 in biofluids represents a major limitation for its use as diagnostic biomarkers and requires the implementation of more challenging detection methods³⁸. Recently, an ELISA test detected TDP-43 in CSF at concentration below 0.49 ng/mL³⁴ and a detection limit of 0.5ng/mL³⁹ has been achieved in serum using an electrochemical sensor. However, quantification of TDP-43 in CSF and plasma results highly variable across studies^{38,40} and the large part of patients and healthy subjects show TDP-43 levels below the detection limit of the typical immunoassays^{36,37}. In this respect, more sensitive assays are required to measure low TDP-43 concentrations present in body fluids for a more accurate validation of this biomarker and even for early diagnosis of ALS and FTLD.

Our sensor demonstrated to detect TDP-43 concentrations down to 10fM (corresponding to 0.43pg/mL). Moreover, according to specificity control experiments, our device scheme results robust against non-specific background noise in both dry and liquid environments, providing a fast and real-time detection even in complex body fluids like human serum.

Results

Fabrication and characterization. The biosensing device active area consists of a compact and periodic array of right-handed platinum nanohelices (Figure 2a). The geometrical and structural parameters have been engineered in our former work⁴¹ to achieve optimized chiro-optical effects in the visible spectral range. More details on fabrication process are reported in the Methods section.

Afterwards, in order to build the efficient sensing core-shell scaffolding, we have exposed the nanohelices to oPD for polymerization by means of a cyclic voltammetry (CV) process (see Methods for further details) for the conformal deposition of a thin and compact dielectric polymer shell^{42–44}. Such a functionalization strategy presents many structural advantages. First, the used monomer, the o-pheniledyamine (oPD), is characterized by a self-limiting polymeric growth under anodic oxidation in aqueous solution affording the formation of an ultrathin coating layer (few nanometers), where the aminic groups can be exploited to bind biomolecules. The self-limiting deposition is controlled by the polymer concentration, the buffer composition and the buffer pH in the CV process^{45,46}.

Second, the C affinity to the polymer ensures a homogeneous immobilization of molecules on the helix surface, consisting of an alloy of Pt crystalline nanograins uniformly embedded into an amorphous carbon matrix⁴¹.

The shell morphology obtained on a Pt-nanohelix, grown on-purpose on a copper grid before and after P-oPD coating, has been studied by Scanning Transmission Electron Microscope (STEM) in Z-contrast

mode, as shown in figure 2b, c, d. Figure 2b, obtained by combining both dark (DF) and bright field (BF) acquisition modes, evidences the conformal coverage of the low index polymeric shell around the helix core. High-magnification STEM images of the helix, acquired in dark field mode, before and after the deposition (figure 2c and 2d), show a very high uniformity of the polymeric thin shell throughout the whole helix structures beyond the shining helix core edges (red arrows), with average thickness of 12 ± 2 nm. The random dark/bright contrast visible into the helix core is related to the complex composition of the structure, with platinum grains appearing dark because of the high Z, and carbon matrix, with lower atomic number, appearing bright.

Optical properties of the 3D metal/dielectric core-shell nano-helices. The circular dichroism spectra of both the core and the core-shell systems are calculated by the experimentally measured (see Methods for measurement details) intensity of left and right-handed circularly polarized transmitted light (T_{LCP} and T_{RCP} , respectively), according to:

$$CD = \frac{\sqrt{T_{LCP}} - \sqrt{T_{RCP}}}{\sqrt{T_{LCP}} + \sqrt{T_{RCP}}} \quad (1)$$

The CD spectrum of the bare helix-based sensor exhibits two opposite dichroic bands (D1 and D2 centered at $\lambda_M=500$ nm and $\lambda_m=840$ nm, respectively as shown in figure 3a, blue line) due to hybridization among the chiral dipoles of the helix arms^{47,48}, with a zero dichroism point (ZDP) at $\lambda_{ZDP}=600$ nm. After the shell deposition, a spectral redshift of the CD bands occurs because the refractive index around the nanostructure increases (figure 3a red line). The unpatterned substrate remains barely affected by such a thin dielectric layer deposition (figure S1 in the Supporting).

Core-shell nanosystems combining materials with different sign permittivities (i.e., metals with dielectrics) are expected to exhibit different effects on absorption and scattering at their resonance frequency, and to modify the electric field distribution around the nanostructures^{49–51}. This depends on the relative core-shell size and on the interplay between nanostructure shape and size and inspecting wavelength. In our specific case, a decay length of 128nm is expected for the plasmonic field⁵² at the CD peak of 500nm through the shell, by considering the optical dispersion of the Pt-based core⁴¹ and of the P-oPD shell (Supporting figure S2). Therefore, we can assume that the measured shell thickness of 12nm still supports the plasmon propagation out to the nanosystem surface.

Moreover, numerical analysis of the near field distribution for both, bare and core-shell nanosystems, at the resonance peaks for the two incident CPL components (λ_{LCP} and λ_{RCP}), (figure 3 b, c) show that the electric field hot spots, close to the metal/air interface in the bare helix, move towards the shell/air interface in the core-shell system. In such positions the field intensity is also increased, thus suggesting a stronger interaction with surrounding biomolecules.

This beneficial contribution to system sensing capabilities is also evidenced by the experimental scattering spectra of RCP and LCP light, measured for the bare single helix, and after the deposition of the

outer shell(Figures 3d-e). Along with the slight spectral redshift, in line with what observed from the CD spectra, the core-shell architecture, when incident CPL matches the structure handedness, induces an enhancement of the scattering intensity, by a factor of 1.1 with respect to the bare core. This enhancement further increases by a factor of 3 with the opposite incident handedness. The results are in agreement with the numerical simulations of the scattering intensity in the supporting figure S3. These two interrelated effects, the enhanced electric field and the increased far field scattering, could be attributed to the energy transfer between polarization charges of the dielectric shell and free electrons in the plasmonic core^{53,54}. As seen later, with respect to biosensing application, the resulting interaction of polymer-coated helices with biomolecules can be more efficient, if compared with other monolayer-thin bioconjugation schemes.

Sensor characterization. A first assessment of the core-shell system sensitivity was performed by measuring the CD in a known refractive index environment, that is glycerol–water mixtures varying concentration from 0 to 20% (corresponding to a refractive index range between 1.333 and 1.358)⁵⁵, as shown in figure 4a, b, c.

The refractive index sensitivity, calculated from the linear fits as $S=\Delta\lambda/\Delta n$ (where $\Delta\lambda$ represents the wavelength shift and Δn the change of the refractive index of the glycerol-water solution), is reported for both λ_M (squares) and ZDP (rhombs) in figure 4d. ZDP exhibits a higher sensitivity ($S=766\text{nmRIU}^{-1}$) and a larger figure of merit ($\text{FOM} = S/\delta\lambda$) up to 1276 RIU^{-1} with respect to λ_M ($S=316\text{nmRIU}^{-1}$ and $\text{FOM}= 235\text{RIU}^{-1}$) confirming the tracking efficiency of the zero dichroism point for molecular sensing^{25,56}. A comparison with state of art performances for LSPR-based systems³¹ demonstrates the large potentiality for the proposed biosensing approach.

The system was then tested for biomolecular recognition (see Methods for details) after antibody immobilization with glutaraldehyde (acting as crosslinker agent between the aminic groups of the polymeric shell and the antibody) and after the incubation of TDP-43 antigen. Analyte measurements at different concentration were then performed in dry medium (see Supplementary S4 for details)^{57–59}.

We have measured the difference of the CD spectral features (Figure 5a) acquired after the antibody layer incubation and after the TDP-43 binding at different molar concentrations, ranging from 1pM down to 10fM, therefore beyond the interval accessible for this analyte through typical immunoassays^{38,39}. ZDP (figure 5b) confirms a larger CD redshift as compared to the maximum ()and the minimum ()CD features (figure S5). The linear trend of the spectral shifts as a function of the molar concentration is noticeable in figure 5c, with a concentration sensitivity of 27nm/pM.

Specificity and imperturbability. The real optical and biochemical effectiveness of our functionalization method has been tested by comparing the TDP-43 detection results with the standard approach based on the self-assembly monolayer of thiols, commonly used for metallic surfaces, including platinum^{60,61}. In the thiols- based functionalization experiment (see methods for details), the detected ZDP redshift for an analyte concentration of 1pM was 5nm (figure S6), five-times lower than the value obtained with the core-

shell architecture (27nm, Figure 5). This result comes from the combination of the core-shell optical properties discussed above with the fact that, while thiols layer-binds only to the Pt grains in the complex helix material alloy leaving the carbon surface fraction uncovered, the polymeric shell conformally coats the entire helix surface. This allows to maximize the total specific binding sites available for the target analyte and to amplify the detected signal.

In addition, the sensor specificity has been tested performing two control experiments. In the first case, we have used our nanohelix-based sensor with immobilized antibodies for TDP-43 on the polymeric shell, to reveal the non-specific detection of Tau protein, a biomarker related to Alzheimer Disease (AD) and Parkinson Disease (PD) neurodegenerative diseases⁶². The sensor has been incubated with a solution of Tau protein at 500 fM molar concentration. As shown in figure 6a that compares the chiroptical measurements before and after the antigen deposition, the multiple CD spectral features show no distinct variation on addition of non-target Tau protein, because no specific binding events occur, demonstrating that the nano sensor is selective and specific to target molecules.

The second experiment consists to detect the TDP-43 in the complex environment of human serum, characterized by the presence of different biomolecules that can potentially interfere with the specific analyte detection. The results are shown in figure 6b, where the CD features are recorded (i) only with the immobilized TDP-43 antibody, (ii) after the addition of human serum and (iii) after the addition of human serum spiked with TDP-43 (at 500fM), respectively. While the human serum acting as background does not induce distortion in the CD signatures, the addition of the spiked serum leads to significant ZDP redshift of about 15nm, the same value recorded in the detection of pure TDP-43 with the same concentration (500 fM) (figure 5).

Moreover, the possibility offered by our chiral sensor to use the CD spectrum introduces the additional property of the unperturbability to signals coming outside the active area. Indeed, considering that the thin layer of p-oPD is also deposited on the substrate, it creates binding sites for antibody-antigen pairs, generating the same transmission offset for both the circularly polarized transmitted lights, that the CD can delete because it is a differential signal. These results point out the excellent and stable performances and the reliability of the device.

Discussion

In summary, we engineered an ordered array of three-dimensional core-shell chiral nanostructures to be considered as novel chip-based optical biosensing concept. We analytically and experimentally demonstrated the sensing capabilities of our system owed to the combination of a metallic core of 3D chiral nano-helices conformally coated by a thin layer of dielectric polymer.

The high sensing performances are achieved thanks to the combination of many factors, namely: (i) the third dimension, which ensures a large binding area; (ii) the intrinsic chiral shape, which makes the sensor stable against the background interference and, consequently, suitable to work on optically dense

environments like body fluids; (iii) and the polymer-mediated functionalization, which provides additional advantages. On one hand, it creates a homogeneous and large surface for biorecognition. On the other hand, from an optical standpoint the metal-dielectric core-shell system enhances the scattering signal due to the interaction between polarization charges of the dielectric shell and free electrons of the plasmonic core. First of all, the engineering of such device provides refractive index sensitivity related to CD spectral features of about 800nm/RIU, which is among the highest achieved with LSPR-based sensors. Then the sensor has been tested by evaluating the shift in due to the presence of TDP-43, whose identification at low concentration in body biofluids can help in the fight against neurodegenerative diseases. In a low concentration range, between 1pM and 10fM, the sensor shows a linear behavior with a CD shift of 27nm for TDP-43 picomoles.

Our platform also demonstrated a high specificity toward the target biomarker with very low signal due to aspecific interaction of bioreceptor with other molecules such as Tau protein that is a biomarker related to different neurodegenerative disease: it would be of great importance from a clinical point of view since it would allow to distinguish between ASL and other neurodegenerative diseases.

Further improvement in sensitivity can be envisioned thanks to the size-, geometry- and material-dependent engineering of the sensor, leading to even more pronounced bisignated circular dichroism, with steeper stop bands, for larger and easier-to-detect spectral shifts. Thanks to the chip-based approach our device could be integrated with microfluidic tools, including for example sample preparation module, to separate human serum from a single drop of blood, to achieve a fully automated platform. In addition being a miniaturized photonic component, it can be embedded within a portable point of care system, with a simple integrated optical read out, considering that it works in transmittance under normal incidence conditions, thus not requiring complex excitation geometries²⁶. Moreover, the demonstration of femtomolar detection of a protein such as TDP-43 and the very low aspecific signal due to the interference of complex matrices of biological fluids impose our analytical approach as an ideal candidate for the detection of blood-circulating protein biomarkers, especially in cancer diagnostics or infectious disease where specific analysis are often complicated both by the low concentrations and by strong interference from serum/blood molecules^{63,64}. This goal can be reached just by changing the recognition element and choosing an appropriate receptor able to bind to the target biomarker.

In addition, the intrinsic chirality of the nanohelices can open perspectives in enantiomeric detection, of critical importance for chemical and pharmaceutical applications. Furthermore, the finding that the core-shell architecture, used for biochemical functionalization, can enhance the near- and far-field optical properties opens wide perspectives to explore novel nanophotonics schemes, not only for sensing but also for fundamental light-matter interactions.

Experimental Section

Sample Fabrication: A series of arrays of 3D Platinum-based Nano-helices single loop with lateral period (LP) 500nm, vertical period (VP) ranging from 450 to 550nm, external diameter (ED) 300nm and wire

radius (WR) 90-120nm, were realized on ITO-on-glass substrate with Focused Ion Beam Induced Deposition technique employing a Carl Zeiss Auriga40 Crossbeam FIB/SEM system. This system allows the realization of 3D structures together with a gas injection system that contains the source of trimethyl-methylcyclopentadienyl-platinum(IV) precursor. The gas is injected in the chamber and the ion beam (with parameters 1pA, 30KeV acceleration voltage and 10nm step size) dissociates the gas molecules to obtain, locally, a controlled and uniform growth of the nano helices array, sized 10x10 μ m. The vacuum chamber was kept within a pressure range from 8.80x10⁻⁷ mbar to 9x10⁻⁶ mbar during the deposition time. To perform the STEM characterization a single helix was grown on-purpose on a copper grid with the same growth conditions of the array.

Optical characterization: Transmission spectra were recorded with an optical microscope Zeiss Axioscope A1 with a home-made confocal system coupled to an imaging spectrometer. Light from a tungsten lamp is focused on the sample with a condenser with NA<0.1 and it is collected using a 40x objective lens with NA<0.95. Then, the light transmitted through the sample is guided through a system made by three lenses that reconstruct, collimate and refocus the real space image. The selected real image is reconstructed and directed to a CCD camera (Hamamatsu Orca R2) coupled with a 200 mm spectrometer for measurements in the visible spectral range and to an InGaAs detector (Princeton Instruments, OMA V InGaAs linear array) coupled with a 300 mm spectrometer in the near-infrared region of the spectrum. Adjustable square slits were used to select the array area. The circularly polarized light has been produced using a combination of a linear polarizer and a quarter-wave plate. For measurements in visible spectral range a linear polarizer and a superachromatic waveplate (Carl Zeiss, 400-800nm) have been used while for measurements in NIR region a linear polarizer (Thorlabs, LPVis100-MP 550nm - 1.5 μ m) coupled to an achromatic quarter wave plate (Newport, Achromatic Waveplate 700-1000nm) have been used. All transmission measurements were normalized to the optical response of the substrate. The scattering spectra of single chiral nanostructure have been performed with a confocal spectrometer (HORIBA LabRam HR) equipped with a cooled charge-coupled device (CCD) Camera (Andor DU 420A-OE 325) and 150 g/mm diffraction grating. The position and visualization of the sample are carried out by another CCD camera (Cannon 400D). For the measurements the following darkfield scheme is implemented. The non-polarized light from a halogen lamp (Ocean Optics HL-2000-HP) connected with 400 μ m Vis-NIR fiber (Ocean Optics), passes through a linear polarizer and superachromatic quarter-wave plate (Thorlabs, 325-1100 nm). Then the incident light is focused by an objective (Mitutoyo Plan Apo NIR, infinity corrected, 10x, NA = 0.26) and obliquely excite the sample with helices at the angle of 65 degrees to the surface normal. The scattered signal is collected by the second achromatic objective (50x, NA = 0.42 Mitutoyo Plan Apo NIR) placed perpendicularly to the sample surface. All scattering spectra are normalized to the lamp spectra measured at the same experimental condition.

Polymer Electrodeposition: The polymer is deposited on the helices surface from a solution of o-PD (SIGMA Aldrich) at a concentration of 0,01mg/mL in the acetate buffer (pH 5) by cyclic voltammetry (with potential ranging from -0.02V to 0.8V, scan rate 50mV/s) with an Autolab PGSTAT 302N. The ITO samples with helix arrays were cut in size 1x1 cm before immersion in the solution.

SEM and STEM images: SEM and STEM characterization was performed by means of a Merlin Zeiss microscope operating in scanning mode on helix array and single helix fabricated on a TEM grid copper by combining dark-field and bright field. In order to obtain Z contrast sensitiveness from the images, STEM was configured in high-angle annular dark-field mode.

Numerical simulation: Finite element method (FEM) simulation was developed through Comsol Multiphysics 5.4, by exploiting wave optics module and carrying out a frequency domain study of electromagnetic waves. All the physical dimensions were evaluated by realizing a geometry consisting of the Pt/C helix, the oPD shell, the air medium around the structure and a perfectly matched layer. Wavelength sweeping was performed in a range between 400 nm and 1000 nm with a step of 10nm, by exciting the structures with circularly polarized light through a background field directed with zenith distance of $\pi/3$, then collecting far field signal along zenith, in a solid angle of 0.7π steradians, according to the experimental setup. The material dispersions used are from ⁴¹ for platinum/carbon alloy and from Supporting Fig. S2 for the polymer shell.

Functionalization procedure: To enable the biorecognition assay, the developed functionalization protocol, after the polymer coating, foresees the incubation with a solution of glutaraldehyde (SIGMA Aldrich) 0.1% (w/v) for 40 minutes: the glutaraldehyde acts as a crosslinker between the P-oPD and antibody's amino groups. Later, the immobilization of polyclonal antibody directed against the C-terminal amino acids of human TDP-43 (Proteintech) was carried out through 1h incubation, with an antibody solution of 2ng/ml in humid conditions in order to avoid the evaporation of the sample drop. Then, the platform was rinsed with water and dried under nitrogen flow. In the control experiments with thiols functionalization the antibodies were immobilized to a self-assembled monolayer realized by the deposition of a mercaptoundecanoic acid (11-MUA) (SIGMA Aldrich) (0.2 mM) in ethanol incubating the sensors with the thiols'solution for 2h. Then the COOH groups of MUA were activated by incubation with a solution of N-hydroxysuccinimide (NHS) (SIGMA Aldrich) and N-ethyl- N-(3-dimethylaminopropyl carbodiimide hydrochloride (EDC) (SIGMA Aldrich) at a ratio of 1:4 in milliQ water for 30 min. Then a solution of antibodies in PBS at a final concentration of 2ng/ml was incubated for 1 h to allow a covalent binding to SAM. To allow the biorecognition between the antibody and the analyte, the functionalized sensors were incubated with solutions of the un-tagged human recombinant TDP-43 protein (amino acids 1-414; Novus Biological) at different concentrations ranging from 1pM (43pg/mL) to 10 fM (0.43pg/mL) in PBS for 30 minutes, then rinsed in milliQ water and finally dried. The incubation process and optical measures were repeated for increasing concentrations of TDP-43. For the specificity tests the functionalized sensor has been incubated with solutions of Tau protein (SIGMA Aldrich) at 500fM in PBS for 30 minutes, then rinsed in milliQ water and finally dried. For the complex environment experiment, the functionalized sensor has been incubated with solutions of TDP-43 (Novus Biological) at 500fM in human serum for 30 minutes, then rinsed in PBS and finally dried.

Regeneration. After optical measurements, the sensors can be regenerated through UV-ozone exposure followed by ethanol rinsing, leading to a weakening and complete remotion of the polymer chain with the linked antibody-antigen pair and returning to original CD spectral features.

Declarations

Acknowledgements

This work was supported by “Tecnopolis per la medicina di precisione” (TecnoMed Puglia) – Regione Puglia: DGR no. 2117 del 21/11/2018 CUP: B84I18000540002. V.T. acknowledges the Short Term Mobility program of CNR. All the authors thank Iolena Tarantini for technical support.

Author contributions. V.T. A.P., M.E., proposed the idea and M. M. and E. P. designed the experiments. M. M. performed the nanofabrication of both single and array nanostructures, and the optical characterization on the nanostructured arrays. E. P. performed the electrodeposition and the functionalization procedure. M. E. and M. C. performed the STEM imaging. Y. S. and D. Z. performed the scattering measurements of the single nanostructures. A. L. carried out the numerical simulations. A. R. and A. Q. provided the TDP-43, the human serum and obtained ethical permission. M. M., M. E., V. T., A. P. analyzed the data. M. M. carried out the original draft preparation. M.M., V.T., M.E., A.P. and E. P have written, and reviewed the paper. All authors participated in the supervision and editing of the draft of the manuscript and approved the final version.

Correspondence and requests for the material should be addressed to M. E., V. T., E. P. (email: marco.esposito@nanotec.cnr.it, vittorianna.tasco@nanotec.cnr.it, elisabetta.primiceri@nanotec.cnr.it)

References

1. Brolo, A. G. Plasmonics for future biosensors. *Nat. Photonics* **6**, 709–713 (2012).
2. Turner, A. P. F. Biosensors: sense and sensibility. *Chem. Soc. Rev.* **42**, 3184–3196 (2013).
3. Mejía-Salazar, J. R. & Oliveira, O. N. Plasmonic Biosensing. *Chem. Rev.* **118**, 10617–10625 (2018).
4. ANKER, J. N. *et al.* Biosensing with plasmonic nanosensors. in *Nanoscience and Technology* 308–319 (Co-Published with Macmillan Publishers Ltd, UK, 2009).
doi:doi:10.1142/9789814287005_0032
5. Stockman, M. I. Nanoplasmonic sensing and detection. *Science (80-)*. **348**, 287 LP – 288 (2015).
6. Liu, J., Jalali, M., Mahshid, S. & Wachsmann-Hogiu, S. Are plasmonic optical biosensors ready for use in point-of-need applications? *Analyst* **145**, 364–384 (2020).
7. Chang, C.-Y. *et al.* Flexible Localized Surface Plasmon Resonance Sensor with Metal–Insulator–Metal Nanodisks on PDMS Substrate. *Sci. Rep.* **8**, 11812 (2018).
8. Sreekanth, K. V. *et al.* Extreme sensitivity biosensing platform based on hyperbolic metamaterials. *Nat. Mater.* **15**, 621–627 (2016).

9. Lee, K. S. & El-Sayed, M. A. Gold and silver nanoparticles in sensing and imaging: Sensitivity of plasmon response to size, shape, and metal composition. *J. Phys. Chem. B* **110**, 19220–19225 (2006).
10. Charles, D. E. *et al.* Versatile Solution Phase Triangular Silver Nanoplates for Highly Sensitive Plasmon Resonance Sensing. *ACS Nano* **4**, 55–64 (2010).
11. Gartia, M. R. *et al.* Colorimetric Plasmon Resonance Imaging Using Nano Lycurgus Cup Arrays. *Adv. Opt. Mater.* **1**, 68–76 (2013).
12. Wang, Z., Cheng, F., Winsor, T. & Liu, Y. Optical chiral metamaterials: A review of the fundamentals, fabrication methods and applications. *Nanotechnology* **27**, 1–20 (2016).
13. Collins, J. T. *et al.* Chirality and Chiroptical Effects in Metal Nanostructures: Fundamentals and Current Trends. *Adv. Opt. Mater.* **5**, 1–46 (2017).
14. Wang, X. & Tang, Z. Circular Dichroism Studies on Plasmonic Nanostructures. *Small* **13**, 1–14 (2017).
15. Schäferling, M., Dregely, D., Hentschel, M. & Giessen, H. Tailoring enhanced optical chirality: Design principles for chiral plasmonic nanostructures. *Phys. Rev. X* **2**, 1–9 (2012).
16. Hendry, E. *et al.* Ultrasensitive detection and characterization of biomolecules using superchiral fields. *Nat. Nanotechnol.* **5**, 783–787 (2010).
17. Kelly, C. *et al.* Chiral Plasmonic Fields Probe Structural Order of Biointerfaces. *J. Am. Chem. Soc.* **140**, 8509–8517 (2018).
18. Lee, H.-E. *et al.* Amino-acid- and peptide-directed synthesis of chiral plasmonic gold nanoparticles. *Nature* **556**, 360–365 (2018).
19. Yoo, S. & Park, Q. H. Metamaterials and chiral sensing: A review of fundamentals and applications. *Nanophotonics* 1–13 (2018). doi:10.1515/nanoph-2018-0167
20. Garcíá-Guirado, J., Svedendahl, M., Puigdollers, J. & Quidant, R. Enantiomer-Selective Molecular Sensing Using Racemic Nanoplasmonic Arrays. *Nano Lett.* **18**, 6279–6285 (2018).
21. Hentschel, M., Schäferling, M., Duan, X., Giessen, H. & Liu, N. Chiral plasmonics. *Sci. Adv.* **3**, 1–13 (2017).
22. Wu, X. *et al.* Unexpected Chirality of Nanoparticle Dimers and Ultrasensitive Chiroplasmonic Bioanalysis. *J. Am. Chem. Soc.* **135**, 18629–18636 (2013).
23. Cai, J. *et al.* Chiral Shell Core–Satellite Nanostructures for Ultrasensitive Detection of Mycotoxin. *Small* **14**, 1703931 (2018).

24. Kumar, J. *et al.* Detection of amyloid fibrils in Parkinson's disease using plasmonic chirality. *Proc. Natl. Acad. Sci.* **115**, 3225 LP – 3230 (2018).
25. Jeong, H. H. *et al.* Dispersion and shape engineered plasmonic nanosensors. *Nat. Commun.* **7**, (2016).
26. A. Paiva-Marques, W., Reyes Gómez, F., N. Oliveira, O. & Mejía-Salazar, J. R. Chiral Plasmonics and Their Potential for Point-of-Care Biosensing Applications. *Sensors* **20**, (2020).
27. Shrivastav, A. M., Cvelbar, U. & Abdulhalim, I. A comprehensive review on plasmonic-based biosensors used in viral diagnostics. *Commun. Biol.* **4**, 70 (2021).
28. Cheng, J.-Y., Yaseen, M. T., Wei, P.-K., Chang, Y.-C. & Moirangthem, R. S. Enhanced localized plasmonic detections using partially-embedded gold nanoparticles and ellipsometric measurements. *Biomed. Opt. Express* **3**, 899 (2012).
29. Manoccio, M., Esposito, M., Passaseo, A., Cuscunà, M. & Tasco, V. Focused ion beam processing for 3d chiral photonics nanostructures. *Micromachines* **12**, 1–28 (2021).
30. Palermo, G. *et al.* Biomolecular Sensing at the Interface between Chiral Metasurfaces and Hyperbolic Metamaterials. *ACS Appl. Mater. Interfaces* **12**, 30181–30188 (2020).
31. Xu, T. & Geng, Z. Strategies to improve performances of LSPR biosensing: Structure, materials, and interface modification. *Biosens. Bioelectron.* **174**, 112850 (2021).
32. French, R. L. *et al.* Detection of TAR DNA-binding protein 43 (TDP-43) oligomers as initial intermediate species during aggregate formation. *J. Biol. Chem.* **294**, 6696–6709 (2019).
33. Hans, F., Eckert, M., von Zweydorf, F., Gloeckner, C. J. & Kahle, P. J. Identification and characterization of ubiquitinylation sites in TAR DNA-binding protein of 43 kDa (TDP-43). *J. Biol. Chem.* **293**, 16083–16099 (2018).
34. Kasai, T. *et al.* Increased TDP-43 protein in cerebrospinal fluid of patients with amyotrophic lateral sclerosis. *Acta Neuropathol.* **117**, 55–62 (2009).
35. Kametani, F. *et al.* Mass spectrometric analysis of accumulated TDP-43 in amyotrophic lateral sclerosis brains. *Sci. Rep.* **6**, 23281 (2016).
36. Foulds, P. *et al.* TDP-43 protein in plasma may index TDP-43 brain pathology in Alzheimer's disease and frontotemporal lobar degeneration. *Acta Neuropathol.* **116**, 141–146 (2008).
37. Verstraete, E. *et al.* TDP-43 plasma levels are higher in amyotrophic lateral sclerosis. *Amyotroph. lateral Scler. Off. Publ. World Fed. Neurol. Res. Gr. Mot. Neuron Dis.* **13**, 446–451 (2012).

38. Feneberg, E., Gray, E., Ansorge, O., Talbot, K. & Turner, M. R. Towards a TDP-43-Based Biomarker for ALS and FTLD. *Mol. Neurobiol.* **55**, 7789–7801 (2018).
39. Dai, Y. *et al.* Application of bioconjugation chemistry on biosensor fabrication for detection of TAR-DNA binding protein 43. *Biosens. Bioelectron.* **117**, 60–67 (2018).
40. Steinacker, P., Barschke, P. & Otto, M. Biomarkers for diseases with TDP-43 pathology. *Mol. Cell. Neurosci.* **97**, 43–59 (2019).
41. Esposito, M. *et al.* Programmable Extreme Chirality in the Visible by Helix-Shaped Metamaterial Platform. *Nano Lett.* **16**, 5823–5828 (2016).
42. Long, J. W., Rhodes, C. P., Young, A. L. & Rolison, D. R. Ultrathin, Protective Coatings of Poly(o-phenylenediamine) as Electrochemical Proton Gates: Making Mesoporous MnO₂ Nanoarchitectures Stable in Acid Electrolytes. *Nano Lett.* **3**, 1155–1161 (2003).
43. Olgun, U. & Gülfen, M. Doping of poly(o-phenylenediamine): Spectroscopy, voltammetry, conductivity and band gap energy. *React. Funct. Polym.* **77**, 23–29 (2014).
44. Losito, I., Palmisano, F. & Zambonin, P. G. o-Phenylenediamine Electropolymerization by Cyclic Voltammetry Combined with Electrospray Ionization-Ion Trap Mass Spectrometry. *Anal. Chem.* **75**, 4988–4995 (2003).
45. Mazeikiene, R. & Malinauskas, A. The stability of poly(o-phenylenediamine) as an electrode material. *Synth. Met.* **128**, 121–125 (2002).
46. Losito, I., De Giglio, E., Cioffi, N. & Malitesta, C. Spectroscopic investigation on polymer films obtained by oxidation of o-phenylenediamine on platinum electrodes at different pHs. *J. Mater. Chem.* **11**, 1812–1817 (2001).
47. Li, Y. R., Ho, R. M. & Hung, Y. C. Plasmon hybridization and dipolar interaction on the resonances of helix metamaterials. *IEEE Photonics J.* **5**, 2700510 (2013).
48. Zhang, Z.-Y. & Zhao, Y.-P. Optical properties of helical Ag nanostructures calculated by discrete dipole approximation method. *Appl. Phys. Lett.* **90**, 221501 (2007).
49. Abrashuly, A. & Valagiannopoulos, C. Limits for Absorption and Scattering by Core-Shell Nanowires in the Visible Spectrum. *Phys. Rev. Appl.* **11**, 14051 (2019).
50. Sheverdin, A. & Valagiannopoulos, C. Core-shell nanospheres under visible light: Optimal absorption, scattering, and cloaking. *Phys. Rev. B* **99**, 75305 (2019).
51. Hassani Gangaraj, S. A., Valagiannopoulos, C. & Monticone, F. Topological scattering resonances at ultralow frequencies. *Phys. Rev. Res.* **2**, 23180 (2020).

52. Cuscunà, M. *et al.* Gallium chiral nanoshaping for circular polarization handling. *Mater. Horizons* **8**, 187–196 (2021).
53. Yu, P. *et al.* Effects of Plasmonic Metal Core -Dielectric Shell Nanoparticles on the Broadband Light Absorption Enhancement in Thin Film Solar Cells. *Sci. Rep.* **7**, 7696 (2017).
54. Avşar, D., Ertürk, H. & Mengüç, M. P. Plasmonic responses of metallic/dielectric core-shell nanoparticles on a dielectric substrate. *Mater. Res. Express* **6**, 65006 (2019).
55. Cheng, N.-S. Formula for the Viscosity of a Glycerol–Water Mixture. *Ind. Eng. Chem. Res.* **47**, 3285–3288 (2008).
56. de Oliveira, T. V. A. G. *et al.* Ultrasensitive and label-free molecular-level detection enabled by light phase control in magnetoplasmonic nanoantennas. *Nat. Commun.* **6**, 1–8 (2015).
57. Yesilkoy, F. *et al.* Phase-sensitive plasmonic biosensor using a portable and large field-of-view interferometric microarray imager. *Light Sci. Appl.* **7**, 17152 (2018).
58. Hernández, A. L. *et al.* How the surrounding environment affects the biosensing performance of resonant nanopillars arrays: Under dry conditions or immersed in fluid. *Sensors Actuators B Chem.* **259**, 956–962 (2018).
59. Shen, Y. *et al.* Plasmonic gold mushroom arrays with refractive index sensing figures of merit approaching the theoretical limit. *Nat. Commun.* **4**, 2381 (2013).
60. Eklund, S. E. & Cliffel, D. E. Synthesis and Catalytic Properties of Soluble Platinum Nanoparticles Protected by a Thiol Monolayer. *Langmuir* **20**, 6012–6018 (2004).
61. Petrovic, B. V, Djuran, M. I. & Bugarcic, Z. D. Binding of Platinum(II) to Some Biologically Important Thiols. *Met. Based. Drugs* **6**, 521864 (1999).
62. Gendron, T. F. & Petrucci, L. The role of tau in neurodegeneration. *Mol. Neurodegener.* **4**, 13 (2009).
63. Malecka, K., Pankratov, D. & Ferapontova, E. E. Femtomolar electroanalysis of a breast cancer biomarker HER-2/neu protein in human serum by the cellulase-linked sandwich assay on magnetic beads. *Anal. Chim. Acta* **1077**, 140–149 (2019).
64. Ahmadivand, A. *et al.* Functionalized terahertz plasmonic metasensors: Femtomolar-level detection of SARS-CoV-2 spike proteins. *Biosens. Bioelectron.* **177**, 112971 (2021).

Figures

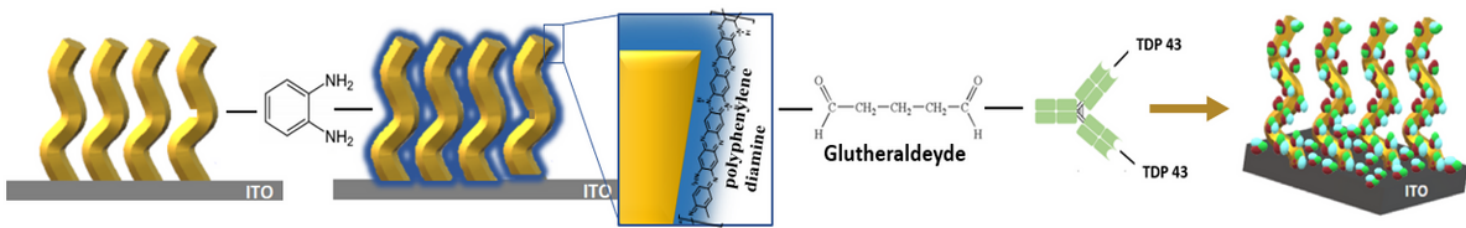


Figure 1

Scheme of the sensing device and functionalization protocol. The core-shell architecture arises from covering the fabricated helix array with the P-oPD insulating polymer. Then, the antibody is immobilized onto the shell after crosslinking by glutheraldehyde. Finally, the target analyte, deposited on the sample surface, is recognized by the specific antibody sites in dry environment.

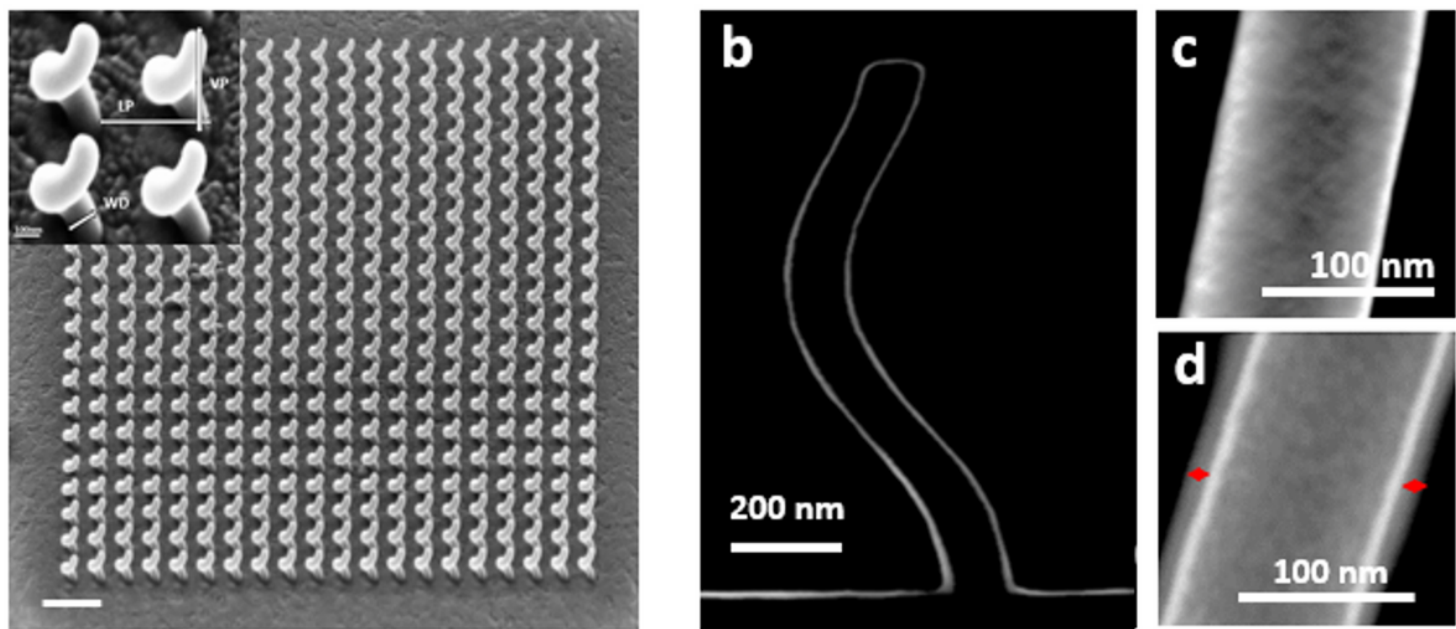


Figure 2

a. SEM image of nano-helix array based active area; the geometrical parameters showed in the inset are lateral period (LP) 500nm, vertical period (VP) ranging from 450 to 550nm, external diameter (ED) 310nm and wire diameter (WD) 120nm. The scale bar is 1um while the scale bar of the inset is 100nm. b. DF+BF High Angle Annular Magnification STEM of a core-shell Pt/P-oPD helix grown on a copper grid highlighting the thin and conformal nature of the P-oPD outer shell. c, d. STEM magnification of a nanohelix section before (c) and after (d) the P-oPD coating. The red arrows indicate the oPD shell thickness of (12 ± 2) nm.

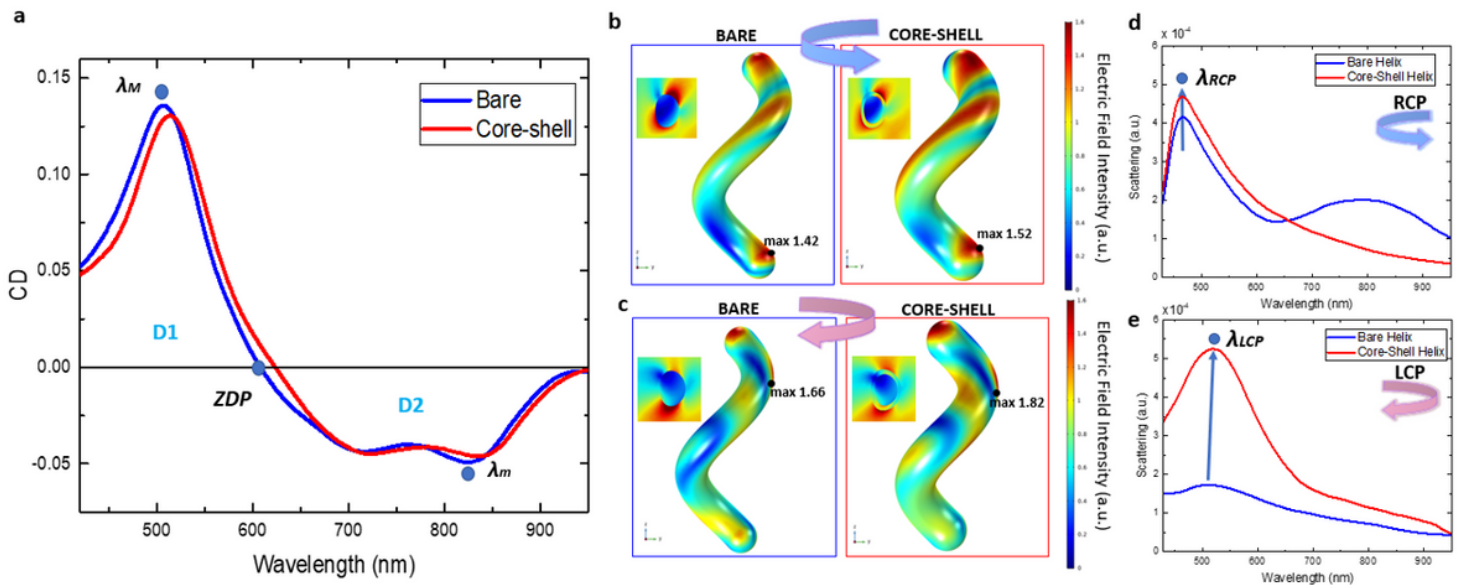


Figure 3

a. CD spectra of nano-helices array before and after shell coating. b, c. Electric field distribution profile for both bare and core-shell single nano-helix calculated at the maximum resonance peak for RCP and LCP, respectively, showing a near field enhancement after shell coating. The insets show the cross section electric field intensity distribution in marked positions. d, e. RCP (d) and LCP (e) scattering spectra measured for a single helix before and after the polymeric shell coating. The curves highlight a strong enhancement of the far field scattering for the core-shell architecture with respect to the core case, by a factor of 1.1 for RCP and 3 for LCP.

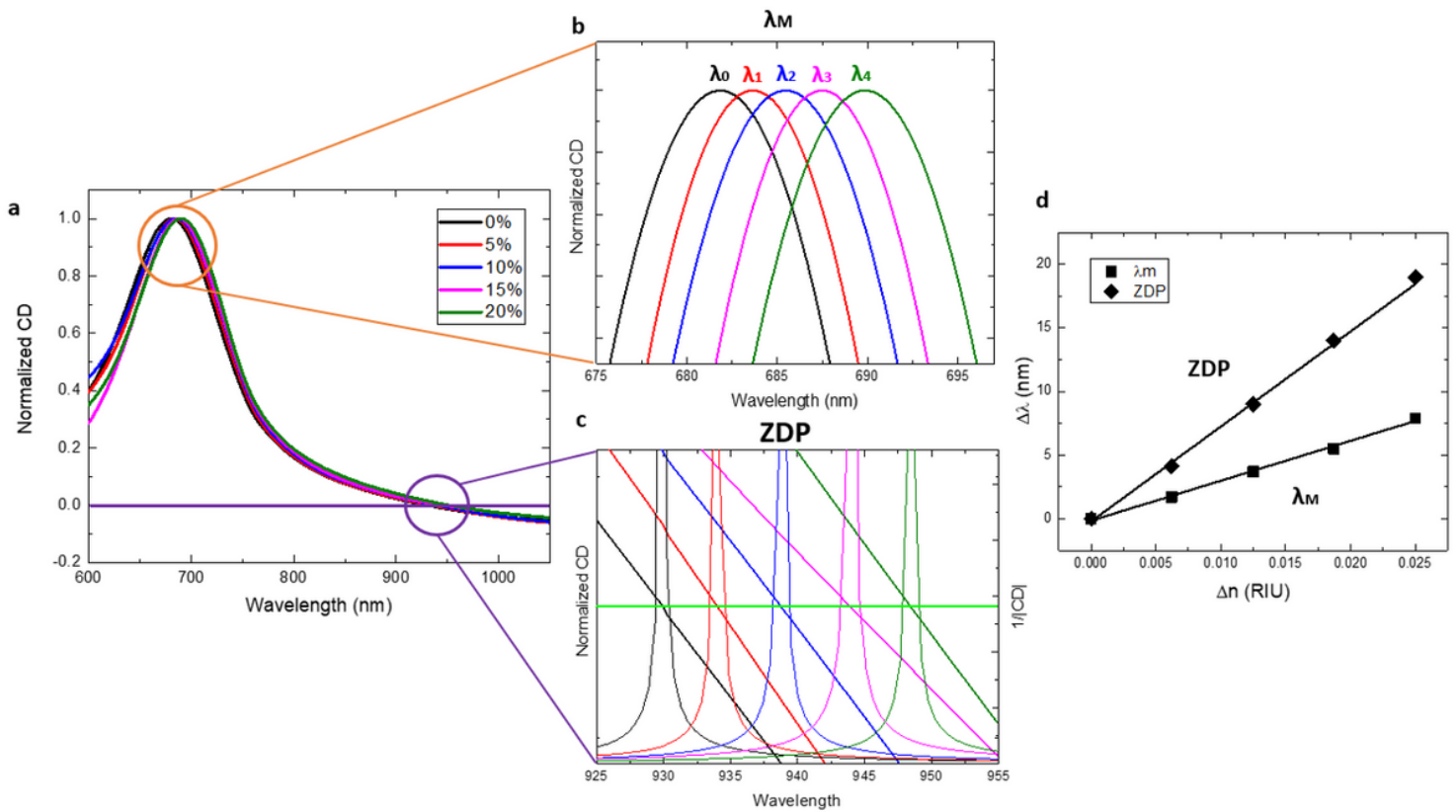


Figure 4

3D metal/dielectric core-shell nano-helices array as refractive index sensor. a. Normalized CD spectra of the core-shell nano-helices immersed in a glycerol-water solution at different molar concentrations. b, c. High-magnification CD spectra for λM (indicated with the orange circle) and ZDP (indicated with purple circle). In particular, $1/|CD|$ is calculated for ZDP in order to evaluate the FWHM values. d. Relationship between λM (black square symbols) and ZDP (black rhombus symbols), and the refractive index. The standard deviation (below 0.4nm) retrieved for the data points falls within the size of the symbols.

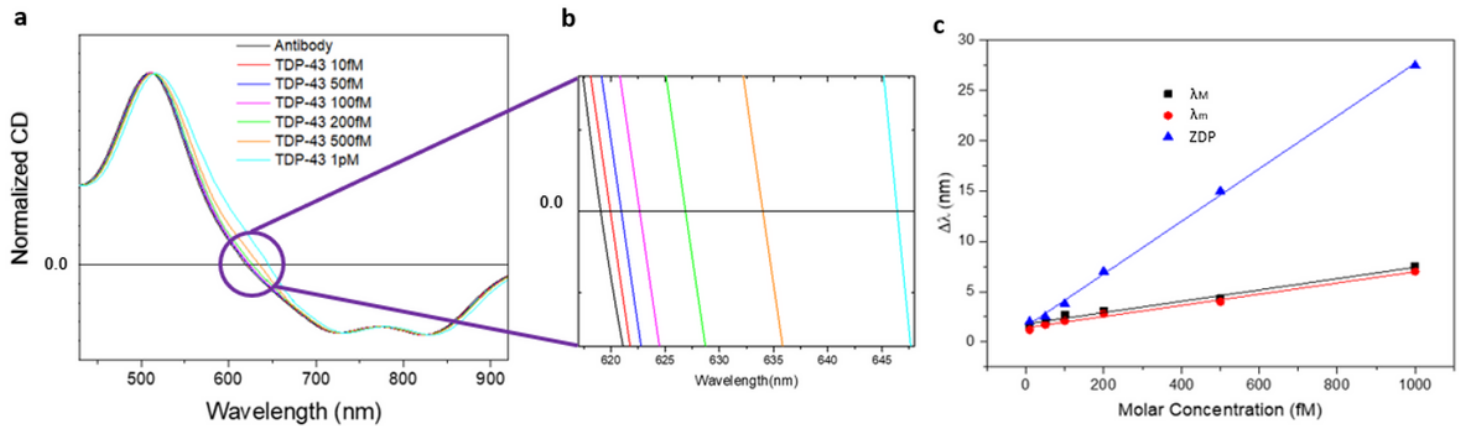


Figure 5

Surface-sensing detection of TDP-43. a. Normalized CD spectra acquired after the only deposition of the antibody layer (spectral reference) and after different concentrations of TDP-43; b. the high-magnification around the ZDP region allows to evaluate the spectral shift of the crossing point between antibody and the antigen at different molar concentrations; c. Linear fit of the spectral shift for λM , λm and ZDP respectively. The size of data points represents the error bars.

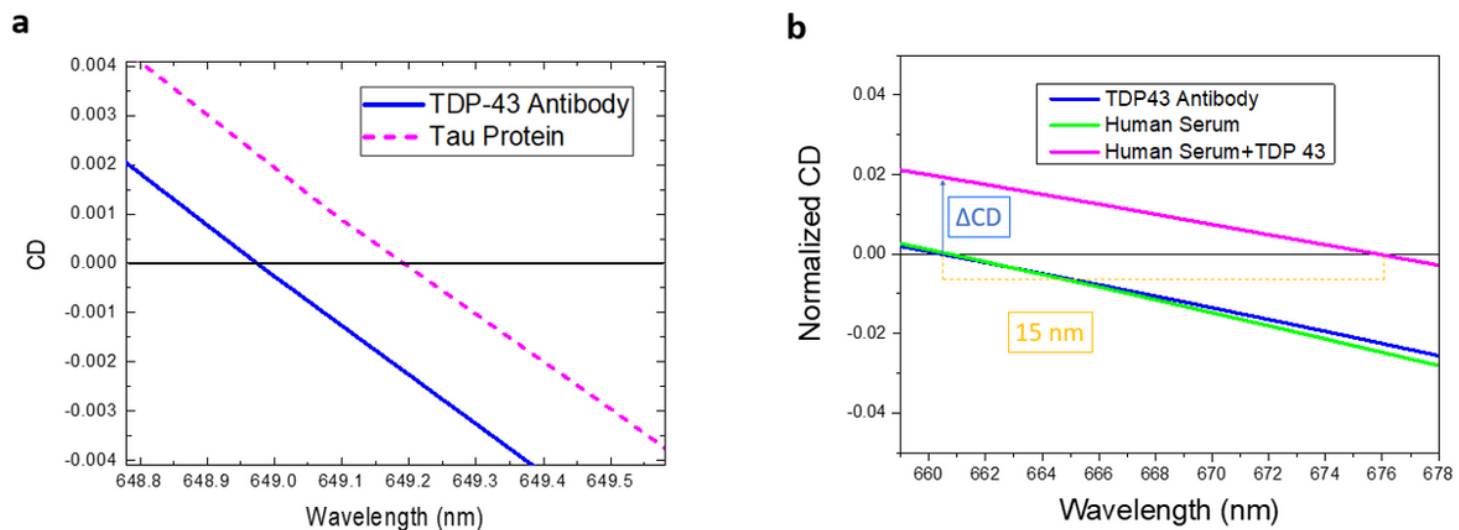


Figure 6

a. Detailed plots of the ZDP for CD spectra acquired after the incubation of TDP-43 antibody (blue curves) and Tau protein (pink dashed line). As depicted by ZDP position, no significant changes are recorded b. Detailed plots of the ZDP for CD spectra measured after the incubation of TDP-43 antibody (blue curves), human serum only (green line) and human serum + TDP 43 (pink lines). Large spectral shift of 15nm is observed only in presence of the target antigen.

Supplementary Files

This is a list of supplementary files associated with this preprint. Click to download.

- [Supporting.pdf](#)